

# Effects of Large-Scale Surface Topography on Ground Motions, as Demonstrated by a Study of the San Gabriel Mountains, Los Angeles, California

by Shuo Ma\*, Ralph J. Archuleta, and Morgan T. Page

**Abstract** We investigate the effects of large-scale surface topography on ground motions generated by nearby faulting. We show a specific example studying the effect of the San Gabriel Mountains, which are bounded by the Mojave segment of the San Andreas fault on the north and by the Los Angeles Basin on the south. By simulating a  $M_w$  7.5 earthquake on the Mojave segment of the San Andreas fault, we show that the San Gabriel Mountains act as a natural seismic insulator for metropolitan Los Angeles. The topography of the mountains scatters the surface waves generated by the rupture on the San Andreas fault, leading to less-efficient excitation of basin-edge generated waves and natural resonances within the Los Angeles Basin. The effect of the mountains reduces the peak amplitude of ground velocity for some regions in the basin by as much as 50% in the frequency band up to 0.5 Hz. These results suggest that, depending on the relative location of faulting and the nearby large-scale topography, the topography can shield some areas from ground shaking.

## Introduction

It has long been known that surface topography can significantly affect earthquake ground motions (Geli *et al.*, 1988). Structures situated at the tops of hills, ridges, and canyons suffer more intensive damage than structures situated at the bases of hills or on level surfaces, as evidenced in past earthquakes such as the 1909 Lambesc, France, earthquake (Angot, 1910), the 1976 Friuli, Italy, earthquake (Brambati *et al.*, 1980), the 1980 Irpinia, Italy, earthquake (Siro, 1982), the 1985 Chile earthquake (Celebi and Hanks, 1986), the 1989 Loma Prieta earthquake (Hartzell *et al.*, 1994), and the 1999 Athens, Greece, earthquake (Assimaki *et al.*, 2005). Higher levels of ground shaking on topographic sites have also been extensively documented from seismic recordings (for example, Shakal *et al.*, 1988, 1994; Hartzell *et al.*, 1994; Spudich *et al.*, 1996; Assimaki *et al.*, 2005).

An abundant amount of theoretical, numerical and experimental work has dealt with the amplification of seismic waves at a topographic site, which has been reviewed by Geli *et al.* (1988) and Bouchon *et al.* (1996). Less attention, however, has been accorded to how topography affects ground motion for nearby sites that are not situated on the topography.

We demonstrate this phenomenon by focusing on the San Gabriel Mountains (SGM)—a macroscopic feature with about 3 km elevation and 30–60 km horizontal expansion

that sits north of the Los Angeles Basin (LAB). The San Andreas fault (SAF), which drives much of the seismic hazard for Southern California (Working Group on California Earthquake Probabilities, 1995; Frankel *et al.*, 2002; Fialko, 2006), slices through the northern boundary of the SGM. The critical feature of this geometry, relevant to this study, is that most of the mountain range lies on the south-southwest side of the fault (Fig. 1). Later we show that the SGM can reduce the severity of the shaking experienced in the LAB from faulting on the Mojave segment of the SAF.

The importance of the subsurface velocity structure on earthquake ground motions has been well documented for basins (Frankel and Vidale, 1992; Olsen *et al.*, 1995; Olsen and Archuleta, 1996; Graves, 1998; Pitarka *et al.*, 1998; Komatitsch *et al.*, 2004; Liu *et al.*, 2004; Krishnan *et al.*, 2006; Olsen *et al.*, 2006). While the effect of the LAB on ground motions has been studied, most of this work neglects a prominent surface feature in the Los Angeles area: the significant topography surrounding the basin. Surface topography has been included in regional (Komatitsch *et al.*, 2004; Liu *et al.*, 2004; Krishnan *et al.*, 2006) and global (Komatitsch and Tromp, 2002a,b) seismic-wave propagation; however, the effects of surface topography on ground motions have not been clearly identified in these studies. Ji *et al.* (2005) attributed the anomalous wave packets recorded by the Southern California Seismic Network during the 2002 Denali earthquake to the reflections of minor-arc Rayleigh waves off the Oregon Coast and the Rocky Mountains.

\*Present address: Department of Geophysics, Stanford University, Panama Mall 397, Stanford, California 94305-2215.

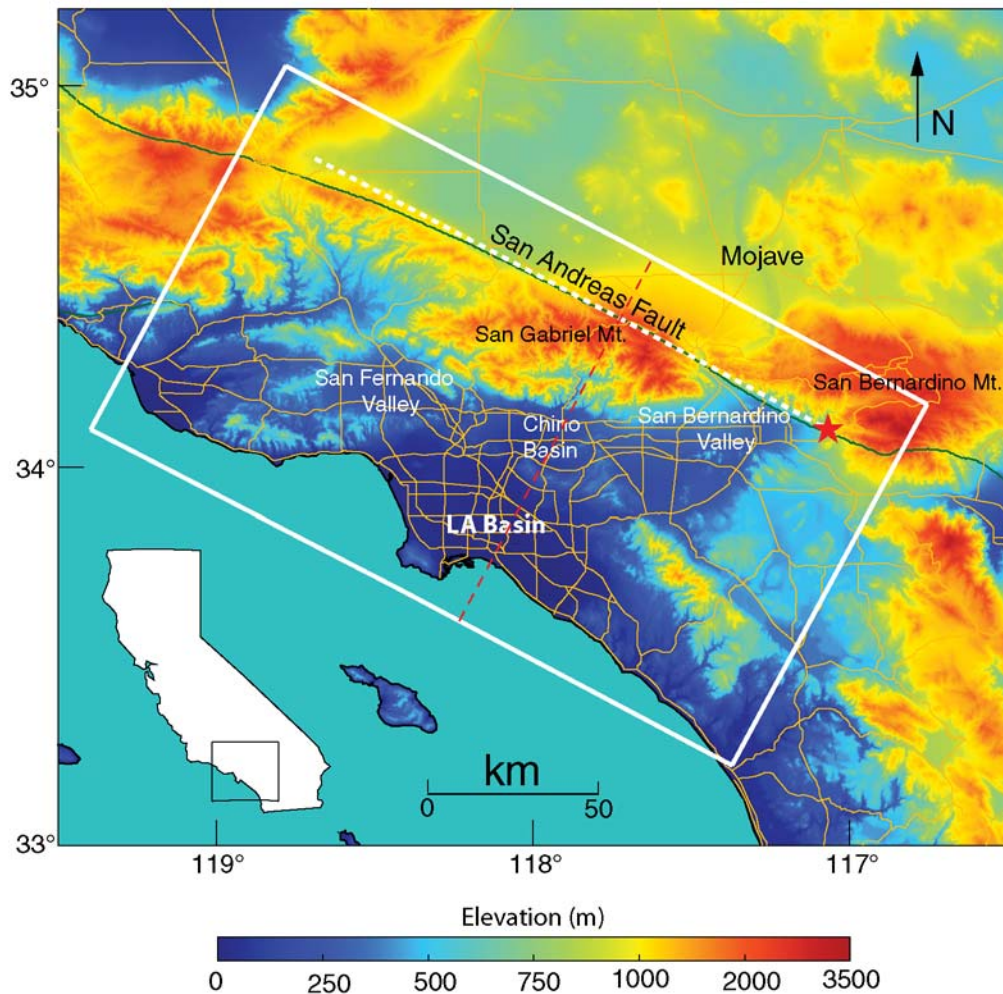


**Figure 1.** Topographic map of the Southern California. The white rectangle shows the surface area of the volume discretized for the simulations. The white dashed line is our approximation to the surface trace of the SAF; the actual trace is the green line. The star denotes the epicenter. The thin yellow lines depict the major highways. In subsequent map-view figures, the rectangle is rotated 28° counterclockwise. The four corners of the white rectangle are (35.052° N, -118.7790° W), (34.099° N, -119.396° W), (33.214° N, -117.369° W), and (34.167° N, -116.752° W). The red dashed line denotes where we show the cross section of the 3D velocity structure in Figure 8.

Surface topography has a more dramatic effect on the propagation of surface waves than that of body waves because of differences in the travel paths. Body waves, elastic waves traveling in the volume beneath the Earth's surface, interact little with surface topography. However, changes in the geometry of the surface of a volume can have a pronounced effect on surface waves. Earlier studies demonstrate that Rayleigh waves can be strongly affected by certain surface irregularities, such as a vertical step (Mal and Knopoff, 1965; Munasinghe and Farnell, 1973; Fuyuki and Nakano, 1984), a rectangular trench (Fuyuki and Matsumoto, 1980), and a semicircular canyon (Wong, 1982; Kawase, 1988), when the wavelength of Rayleigh wave is comparable to the dimension of the irregularities.

To investigate the effect of large-scale topography, primarily the SGM, on ground motion in the Los Angeles area, we simulate a  $M_w$  7.5 earthquake propagating from

San Bernardino to the Tejon Pass on the Mojave segment of the SAF (Fig. 1). This section of the SAF is thought to have caused the 1812 Wrightwood earthquake (Jacoby *et al.*, 1988; Sieh *et al.*, 1989). We isolate topographic effects by simulating a fault rupture and elastic wave propagation and compare the ground motions between models that incorporate the topography in the Los Angeles area and a model without topographic features.

In the following sections, we first study the scattering of a plane Rayleigh wave by a semicircular hill in a homogeneous half-space. We show that scattering by the hill always diminishes the amplitude of Rayleigh waves in the region beyond the hill. This shielding effect is generally larger as the wavelength of the Rayleigh wave decreases with respect to the radius of the hill. Using the finite-element method of Ma and Liu (2006), we then demonstrate the effects of large-scale topography by simulating ground mo-

tions caused by a simulated  $M_w$  7.5 earthquake on the SAF embedded in both a homogeneous half-space and a 3D velocity structure (Magistrale *et al.*, 2000).

### Scattering of a Plane Rayleigh Wave at a Semicircular Hill

We consider a semicircular hill subjected to a plane Rayleigh wave in a homogeneous half-space (Fig. 2a). The  $P$ -wave velocity,  $S$ -wave velocity, and density are 1732 m/sec, 1000 m/sec, and 1000 kg/m<sup>3</sup>, respectively. We simulate the plane Rayleigh wave by solving the equation of motion in a homogeneous half-space where the initial horizontal displacement at the surface has the shape of a Ricker wavelet with a dominant frequency  $f_0$ . The radius of the hill,  $r$ , is equal to the dominant wavelength  $\lambda_0$  of the Rayleigh wave ( $\lambda_0 = V_R/f_0$ , where  $V_R$  is the Rayleigh

wave velocity). The entire computational model is  $24\lambda_0$  wide and  $10\lambda_0$  deep. We discretize the model by using regular four-node quadrilateral elements in the half-space and irregular elements of the same type in the hill. To ensure the accuracy of the propagation of the Rayleigh wave, the element size is equal to  $\lambda_0/60$  in the half-space and slightly smaller in the hill. The total number of elements and nodes are 869,400 and 871,441, respectively. The absorbing boundary of Lysmer and Kuhlemeyer (1969) is used along the boundary, except at the free surface.

At  $t = 0$ , the Rayleigh wave is  $6\lambda_0$  away from the front corner of the hill (Fig. 2a). After the Rayleigh wave hits the hill, scattering by the hill splits the wave energy into transmitted and reflected Rayleigh waves. Part of the energy is also converted to body waves propagating away from the surface (Fig. 2b). Figure 3 shows the comparison of time histories at two locations in front of and behind the hill. The

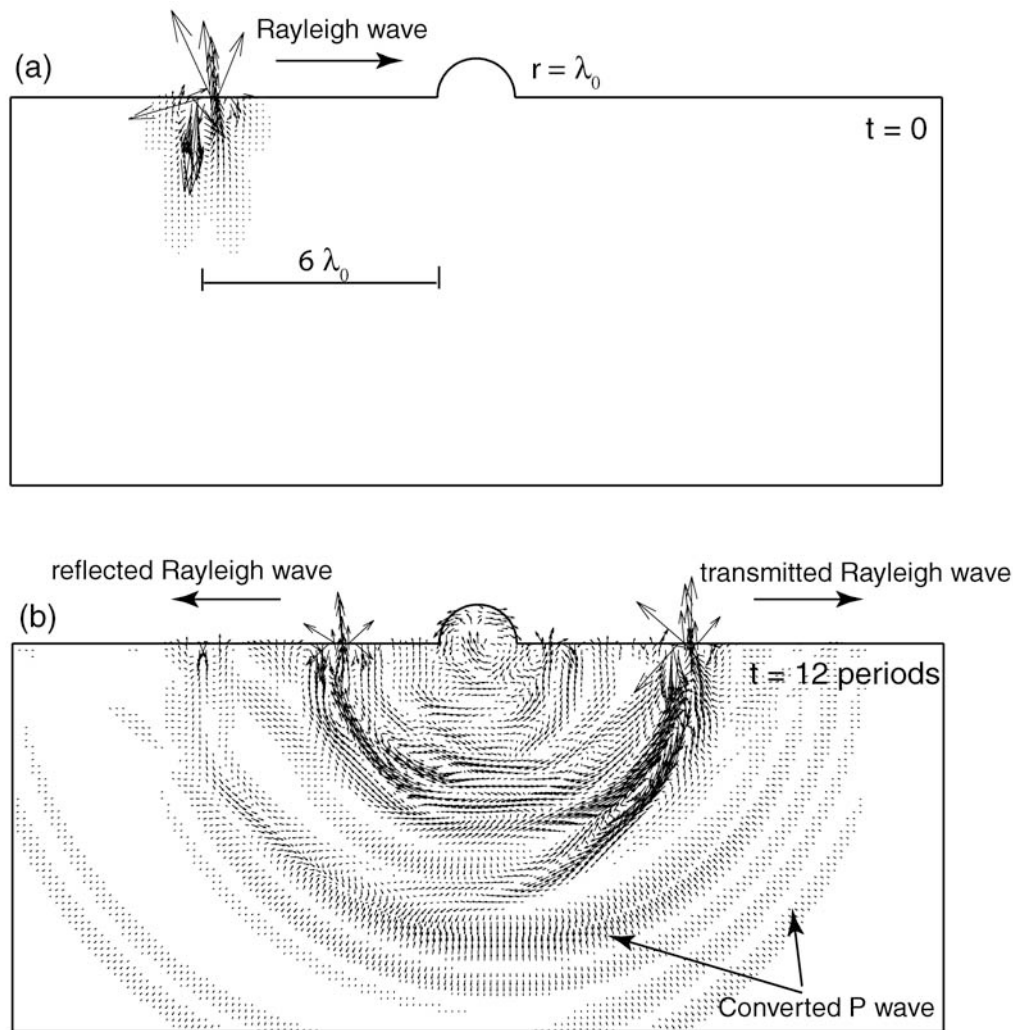


**Figure 2.** Snapshots of the displacement field at (a)  $t = 0$  and (b)  $t = 12/f_0$ . The incident plane Rayleigh wave is strongly scattered at the semicircular hill, and only part of the energy propagates as a transmitted Rayleigh wave. Particle displacement smaller than 1% of the peak horizontal displacement amplitude of the incident wave is not shown. The arrow size in the bottom panel is amplified by two times for better visualization.

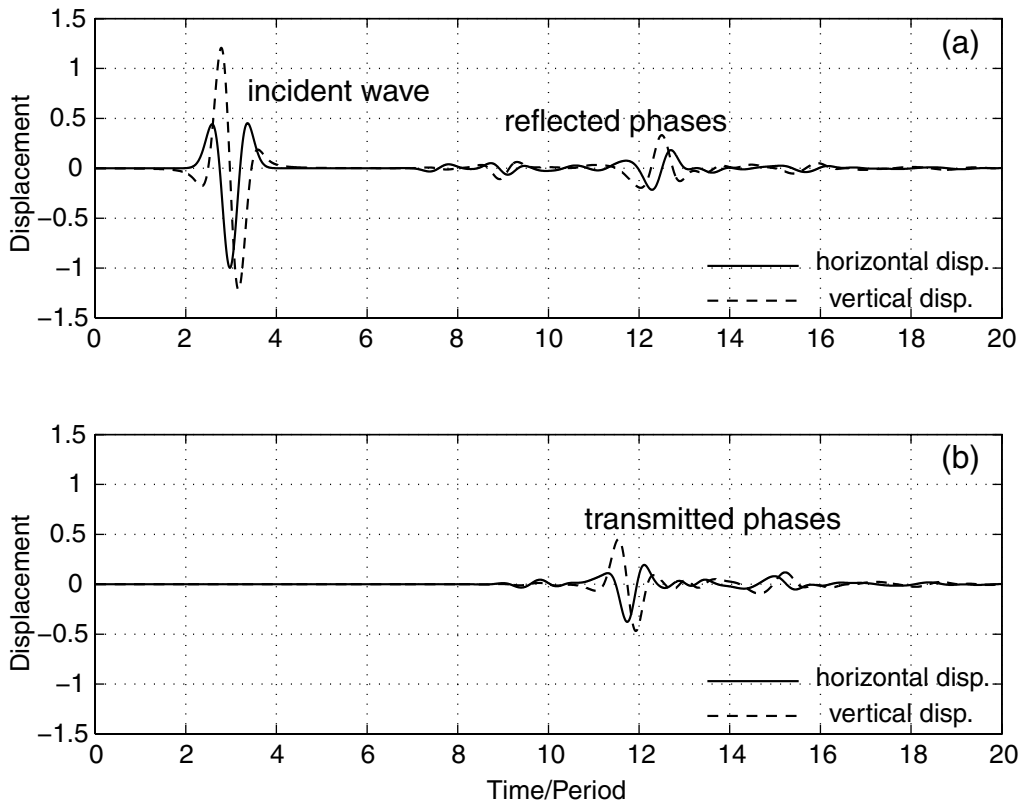


**Figure 3.** Surface displacement time histories at (a)  $x = -4\lambda_0$  and (b)  $x = 5\lambda_0$ . The displacement amplitudes are normalized by the peak horizontal amplitude of the incident Rayleigh wave. The horizontal displacement of the incident wave has the shape of a Ricker wavelet. The amplitudes of the reflected and transmitted phases are significantly smaller than the incident Rayleigh wave due to the scattering at the hill.

peak amplitude of surface displacement behind the hill is reduced everywhere (Fig. 4) indicating that the hill effectively shields this area from the Rayleigh wave. As we vary the dominant wavelength of the incident Rayleigh wave, the shielding effect generally increases as the wavelength decreases relative to the radius of the hill (Fig. 5). When the wavelength of the incident Rayleigh wave is 10 times larger than the radius of the hill, there is still a 16.0% and 13.6% reduction in the peak horizontal and vertical surface displacement amplitudes, respectively. The reduction reaches 61.2% (horizontal displacement) and 53.6% (vertical displacement) as the wavelength decreases to half the radius hill. This simple example illustrates that small convex surface irregularities can strongly affect the amplitude of surface waves.

#### Effects of the San Gabriel Mountains

To investigate the effects of topography and, in particular, the SGM on ground motions in the LAB, we compare results from simulations of ground motion produced by an earthquake on the Mojave segment of the SAF with and without topography. To avoid overly skewed elements in the finite-element mesh for the simulation with topography, we use a spatial running average of 1 km to smooth slightly

the true topography of the Los Angeles area obtained from the 30 m Geographical Information System digital elevation model of Southern California.

We approximate the SAF section as a vertical plane with a constant strike of  $118^\circ$  (Fig. 1). The largest deviation in this fault model from the SAF trace is about 6 km. The fault is 169.6 km long and extends to 16 km below zero elevation. The end points of the fault strike are  $(-118.688^\circ \text{ N}, 34.808^\circ \text{ W})$  and  $(-117.048^\circ \text{ N}, 34.092^\circ \text{ W})$  (Fig. 1). The epicenter  $(-117.068^\circ \text{ N}, 34.101^\circ \text{ W})$  is 2.0 km from the southeast end. The depth of the hypocenter is 10 km below zero elevation. The rupture spreads out radially with a constant rupture velocity of 3 km/sec. Slip is 2.22 m everywhere on the fault with only a strike-slip (right lateral) component. The seismic moment in the 3D velocity structure (Magistrale *et al.*, 2000) without topography is  $2.00 \times 10^{20}$  Nm, corresponding to  $M_w$  7.5. The moment rate function for every point on the fault is a cosine function given by

$$\dot{M}(t) = \begin{cases} \frac{M_0}{T} (1 - \cos \frac{2\pi t}{T}), & \text{if } 0 \leq t \leq T \\ 0, & \text{otherwise} \end{cases}$$

with a width of  $T = 2$  sec.

The fault breaks the Earth's surface for all simulations. Because the elevation at the SAF trace is not zero, the fault

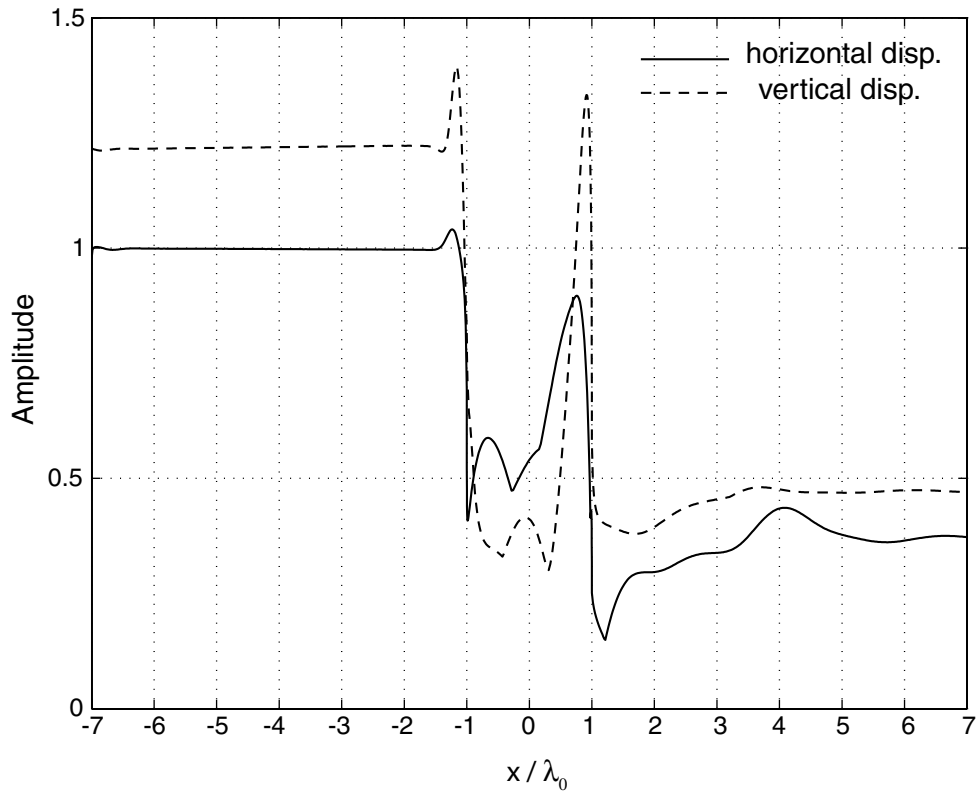


**Figure 4.** Distribution of the peak surface displacement. The displacement amplitudes are normalized by the peak horizontal amplitude of the incident Rayleigh wave. Both peak horizontal and vertical displacement amplitudes are reduced behind the hill. The hill is located at  $-1 < x/\lambda_0 < 1$ .

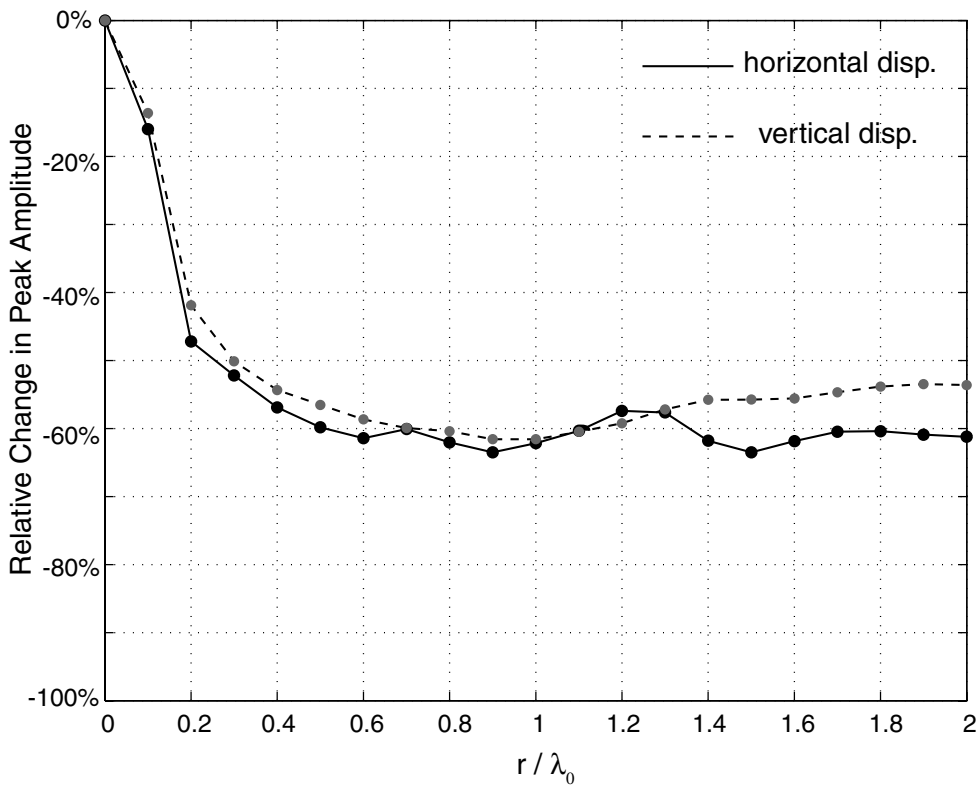


**Figure 5.** Plot of peak surface displacement reductions as a function of wavelength at  $x = 5\lambda_0$ .

area is slightly larger with topography than without topography for a fault that breaks the surface; this results in a slightly larger seismic moment for the simulation with topography.

To simulate the earthquake and the 3D wave propagation, we employ a finite-element method that uses eight-node hexahedral elements with one-point integration and hour-glass control (Ma and Liu, 2006). The method combines both the efficiency of the finite-difference scheme and the flexibility of the finite-element scheme. Ma and Liu (2006) show that the one-point integration scheme allows for a straightforward implementation of the perfectly matched layer (PML) absorbing boundary and the coarse-grained modeling of intrinsic attenuation (Day and Bradley, 2001). In the Appendix we demonstrate the finite-element method's capability for modeling wave propagation in the presence of topography.

We include a large area of Southern California (209.6 km parallel to the strike of the fault by 120 km perpendicular to strike) in all the simulations (Fig. 1). The model extends to depths of 36 km and 46 km below zero elevation for the homogeneous half-space and 3D velocity structure, respectively. The PML absorbing boundary is used for all the boundaries except for the free surface. For simplicity, we do not take into account the intrinsic attenuation.

#### Rupture in the Homogeneous Half-Space With and Without Topography

To isolate the effects of topography we first simulate a SAF rupture with and without topography in a homogeneous half-space. The  $P$ -wave speed,  $S$ -wave speed, and density are 6000 m/sec, 3464 m/sec, and 2700 kg/m<sup>3</sup>, respectively. We discretize both models using a structured hexahedral mesh. The element size is 200 m in the simulation without topography and about 200 m (there are some irregularities in the elements when modeling topography) in the simulation with topography, which gives rise to a total number of 113,184,000 elements and 114,111,269 nodes in both simulations. The total moment in the simulation with topography is 7% larger than without topography due to the 7% increase in the fault area. The timestep is 0.02 sec. We calculate ground motions for 80 sec. All the results are low-pass filtered at 1.0 Hz.

Because we impose a subshear rupture velocity, the fault-normal velocity is larger than the fault-parallel velocity near the fault (Archuleta and Hartzell, 1981). Body waves, which propagate faster than the rupture front, are clearly evident in Figure 6. In the homogeneous half-space, significant energy is also carried by Rayleigh waves—surface waves that are most efficiently generated when there is slip on the shallow parts of the fault. While topography has little effect on body-wave propagation, it significantly scatters the Rayleigh waves and thereby decreases their amplitudes (Fig. 6). The waves scattered off of the topography can be clearly seen in the simulation with topography.

This shielding effect on Rayleigh waves is further demonstrated by comparing the distributions of peak ground velocity (Fig. 7a,b). Near the epicenter, the fault-normal velocity varies along strike because initially the  $S$  waves are radiated from a circularly expanding rupture front, while later the  $S$  waves are radiated from a propagating planar rupture front. The peak amplitude eventually approaches a constant amplitude along strike. In regions where Rayleigh waves dominate the peak amplitude, the peak ground velocity is reduced. Body waves dominate the peak ground velocity in the regions where the relative change in peak ground velocity is small. The regions with larger ground motion (red regions in Fig. 7b) are those where there is amplification on the topography or where waves are scattered (reflected) off of the mountains on the northeast side of the fault. Normally this area near the fault is nearly nodal for the fault-parallel and vertical components when there is no topography. Consequently, the reflected waves dominate the amplitudes of the fault-parallel and vertical components in this region.

To illustrate further how the topography affects the ground motion, we plot the particle velocity time histories at six sites (Fig. 7c). Topography has little effect on body waves. Topography reduces the amplitude of the Rayleigh waves everywhere; this is clearly evident on the vertical component where the Rayleigh wave dominates the peak amplitude (except at site 1 where scattered waves dominate). In time histories where body waves dominate the peak amplitude, the Rayleigh wave component is also reduced (for example, see the fault-normal components at sites 4, 5, and 6). The large pulse near the end of the fault-parallel component at site 6 is the stopping phase of the rupture, which is predominantly an  $S$  wave on which surface topography has little effect. The selective reduction of body waves and Rayleigh waves by the topography together with different radiation patterns of body waves and Rayleigh waves from the fault give rise to the pattern of relative change in peak ground velocity shown in Figure 7b.

#### Rupture in 3D Velocity Structure With and Without Topography

Next, we increase the complexity of the problem by including the 3D velocity structure of the basins (Magistrale *et al.*, 2000). Again we generate two models—with and without the topography. The velocity model has built-in topography. For the simulation without topography, we compress materials above zero elevation down to zero elevation; in this way we do not lose the effect of shallow subsurface structure. Figure 8 shows a cross section of the velocity model with and without topography, which illustrates the slight distortion that arises from the compression in the velocity structure for the simulation without topography; this is most evident for areas with high elevation. The compression of mountainous materials below zero elevation in general leads to a smaller material velocity contrast along basin edges near

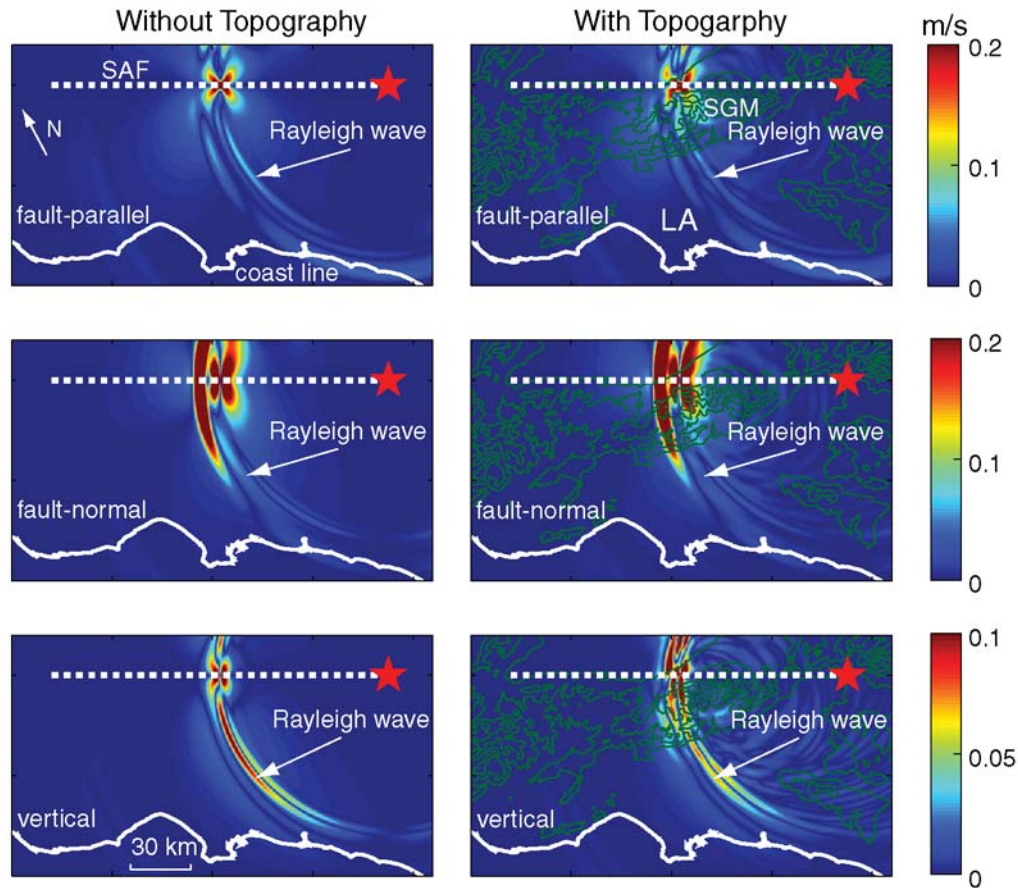


**Figure 6.** Snapshots of the absolute amplitude of three components of particle ground velocity at time  $t = 30$  sec without topography and with topography resulting from rupture propagation on the SAF in a homogeneous half-space. The color scale is saturated in this figure and in all subsequent map-view figures to better highlight features. The red star denotes the epicenter. The contour lines in this figure and subsequent figures show the topography. The amplitudes of the Rayleigh waves are decreased due to scattering by topography. The scattered wavefronts can be seen in the right panels.

the surface because more rigid materials move to a greater depth, which causes a weaker generation of basin surface waves and thus underestimates ground motion in the basin. This is, however, how material properties are normally included in simulations that neglect surface topography.

In each simulation, the minimum  $S$ -wave velocity is 500 m/sec, and the maximum frequency is 0.5 Hz. We discretize the volume using a slightly unstructured finite-element mesh (see fig. 7 in Ma and Liu, 2006). The mesh is mostly structured; unstructured elements are used only in the vertical velocity transition zones where the element size can be increased with depth. A similar mesh has been widely used in the spectral-element simulation of wave propagations (for example, Komatitsch *et al.*, 2004). The element size is about 100 m near the surface and is doubled three times with depth (with three transition zones) so that the element size is about 800 m near the bottom of the model, resulting in a total number of 110,511,600 elements and 112,013,788 nodes for both models. The seismic moment with topography is 8% larger than that without topography

due to a slightly larger fault area and heterogeneity of the velocity structure. The timestep is 0.01 sec. We compute ground motion for 120 sec.

The fault rupture initiates near the edge of the San Bernardino Valley. As soon as the seismic waves hit the basin edge, strong surface waves are generated due to large velocity contrasts (Fig. 9). These basin-edge generated surface waves, predominantly Love waves, continue to be generated at the edges of the basins near the base of the SGM and propagate through the Chino Basin into the LAB. The basin surface waves propagate to the southwest and strongly shake the LAB even after 100 sec.

A clear Rayleigh wavefront is not seen in the basins, but it is a major contributor to the generation of basin-edge-generated Love waves. The propagation direction of the Rayleigh wave (also the direction along which the particle motion of the Rayleigh wave is polarized, see the purple arrow at 40 sec) is approximately east–west (see also Fig. 6 for Rayleigh waves in the homogeneous case). This is almost tangential to the base of the SGM, which is also the basin

edge. When a Rayleigh wave is incident at the basin edges in the 3D velocity structure, the parallelization of the polarization of Rayleigh waves and basin edges strongly favors the conversion of Rayleigh waves into basin Love waves whose particle motion also aligns with the edges of the basin (Fig. 9). The polarization of particle motions remains the same while the wave type changes from the Rayleigh wave

(*P*-*SV* type) to the Love wave (*SH* type). This is a consequence of the specific orientation of the basin in this 3D wave-propagation scenario.

In both simulations, large ground motions in the basins illustrate that the subsurface velocity structure is the dominant factor for ground motion (Fig. 10). However, when topography is included, peak ground velocities for all

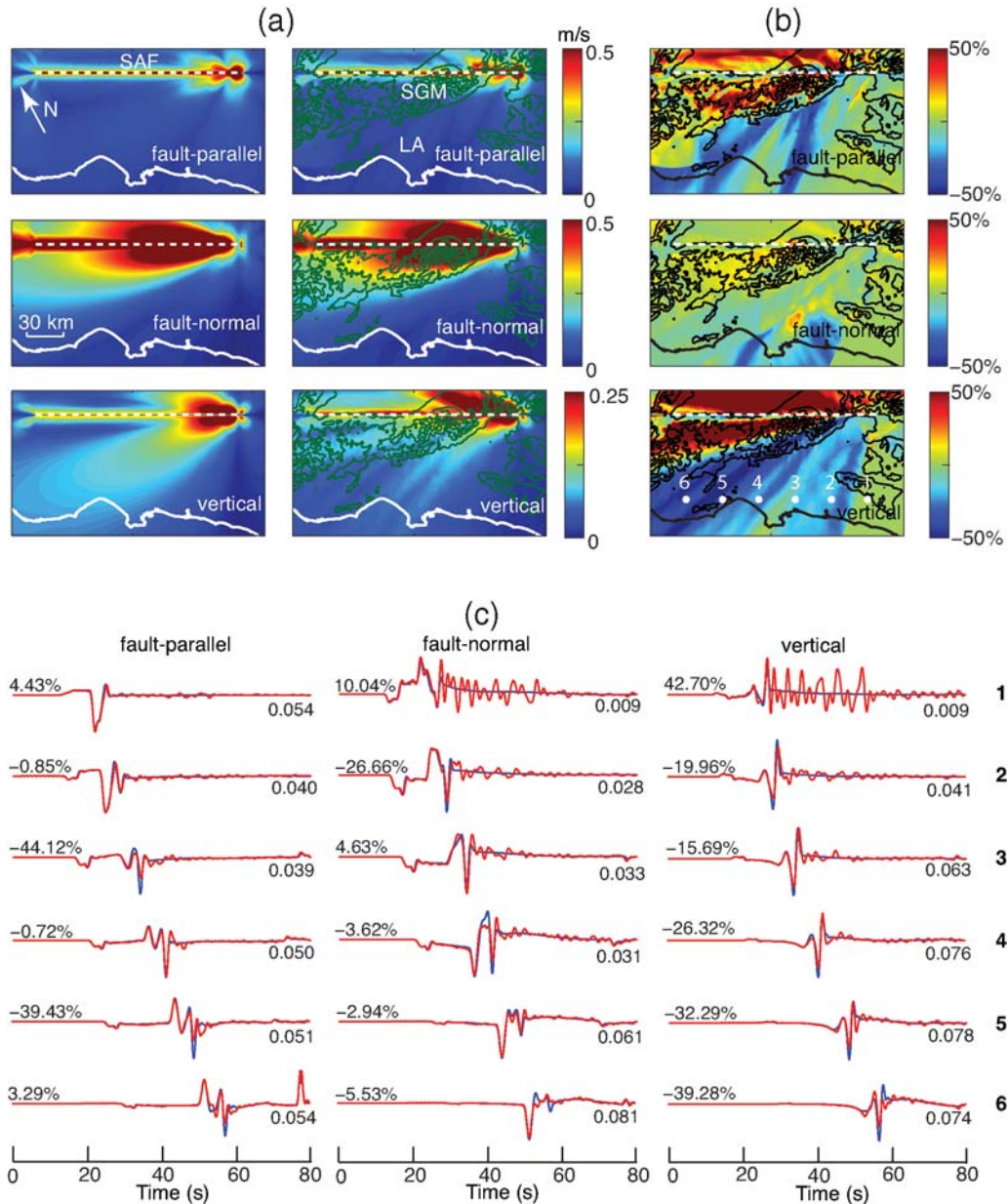


**Figure 7.** Comparison of peak ground velocities in a homogeneous half-space. (a) Peak ground velocities without topography (left-hand column) and with topography (right-hand column). (b) Plots of the relative change between simulations of peak ground velocity with and without topography for locations where the peak velocity without topography is greater than 0.02 m/sec. At locations where the peak velocity without topography is less than 0.02 m/sec, the relative change is set to zero. The white dots in the bottom panel denote the sites where we show seismograms in (c). (c) Comparison of velocity time histories without topography (blue) and with topography (red). The relative change of peak velocity between models with and without topography is shown at the upper left of each trace. The peak-velocity amplitude without topography is shown at the lower right of each trace in m/sec.

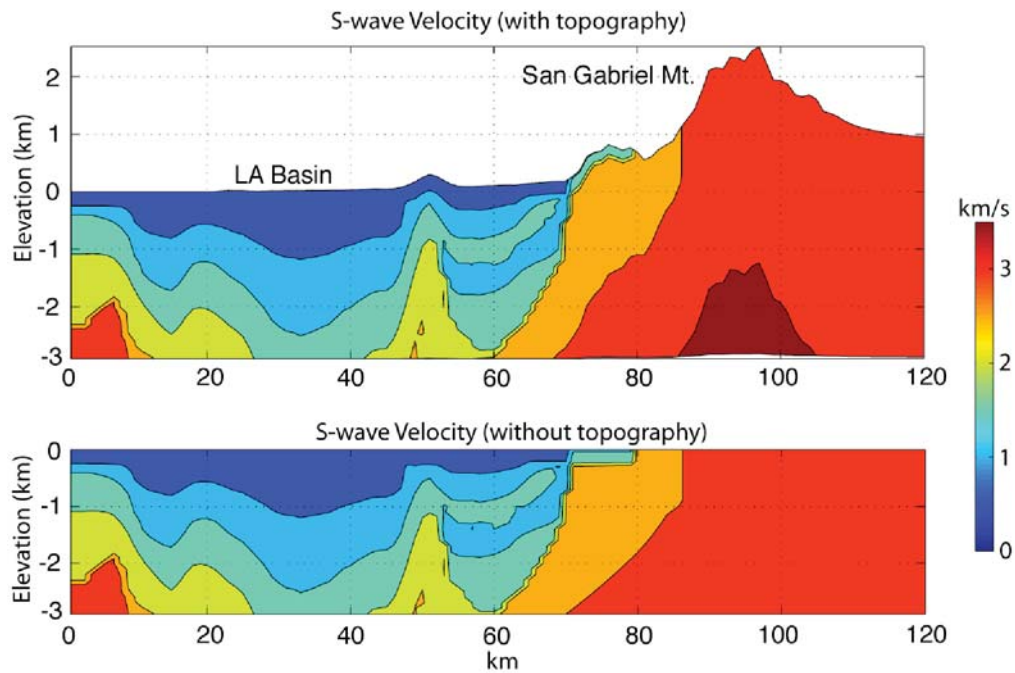


**Figure 8.** Comparison of the 3D velocity model (Magistrale *et al.*, 2000) with and without topography along the cross section denoted in Figure 1.

three components are reduced on the order of 20%–30% in most areas of the San Bernardino Valley, the Chino Basin, and the LAB (Fig. 11a). In some areas the reductions reach as much as 50%. When topography is included, the area northeast of the SAF experiences higher ground motion because some energy is reflected off of the SGM and into the Mojave.

For four basin sites (Fig. 11a), we plot velocity time histories (Fig. 11b) to illustrate the effect that topography has on the ground motion. Site 1, located at the northwestern edge of the LAB, is near the SGM. The peak ground velocity at this station is dominated by fault-generated surface waves, whose amplitudes are strongly reduced after crossing the SGM. At site 4, located near the southeastern edge of the basin, there are strong reverberations polarized on the horizontal components—an indication of basin Love waves generated at the basin edge. The reduction in the amplitude of basin Love waves is due to the reduced excitation (caused by the topography) at the basin edge. At sites 2 and 3 there are increases in the amplitude of several components. At site 2 there is a reduction in peak-velocity reductions on the two horizontal components while the peak vertical velocity has an increase of 5.17%. Likewise at site 3 the peak amplitude increases by 13.15% on the fault-normal component and by 14.31% on the vertical component while the peak fault-parallel velocity is reduced by 28.33%. These peak-velocity increases give rise to the sporadic red dots in Figure 11a. Note that in all cases the phase is undisturbed, indicating that the effect is due to topography—the only difference between the two

simulations. When the amplitude of one component reaches maximum, where the peak amplitude in the simulation with topography increases, we see that the amplitude reduces on the other component(s) at these two basin sites. This suggests that the wave energy is converted from one component to the other due to the topography—typical features of wave-scattering phenomenon. It is well known that scattering can destroy coherent wave propagation and split wave energy into different wave types and polarizations. Therefore, the scattered phases due to the topography can cause constructive interference in some components whose amplitudes are normally much smaller and thus produce a relatively large peak-velocity increase. The same phenomenon can also be seen at site 3 in the homogeneous case (Fig. 7c), where the peak ground velocity increases for the fault-normal component but decreases for the other two components. In looking at the variation among the four sites, however, one observes that the topography generally reduces the peak amplitude of the ground motion.

Although in the simulation with topography a slightly larger seismic moment and a slightly stronger velocity contrast at the basin edge tend to increase the radiation, the effects of topography generally reduce peak ground velocity in most areas of basins. The scattering of fault-generated surface waves caused by the topography leads to less excitation at the basin edges, resulting in the reduction of ground motion in almost the whole basin; these reduction patterns are drastically different from those in the homogeneous case (Fig. 7b). Moreover, the total energy coming into the basins,

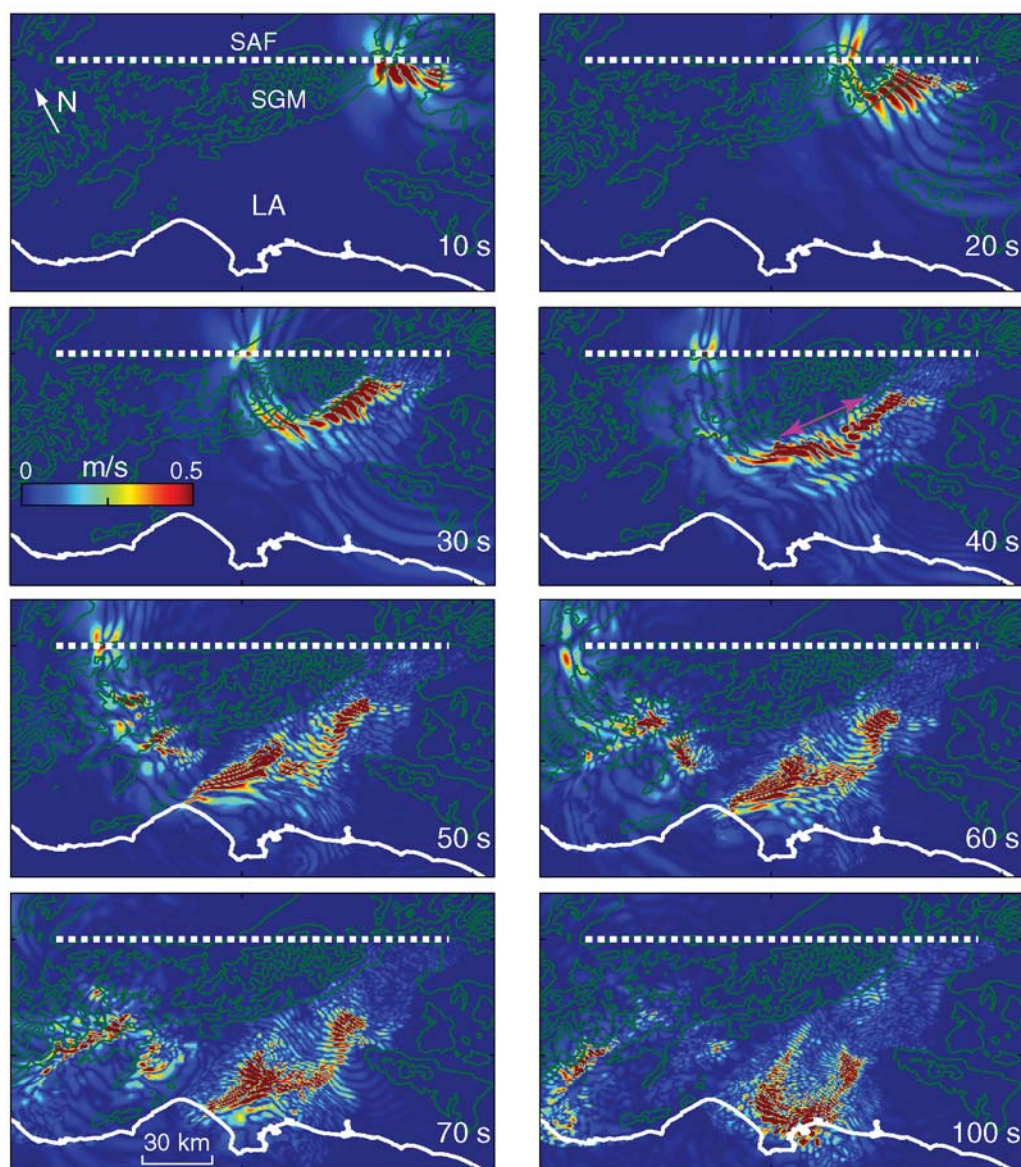


**Figure 9.** Snapshots of the absolute amplitude of fault-parallel particle ground velocity as the rupture propagates along the SAF in the 3D velocity structure with topography. (Note: The amplitude scale is saturated.) Large basin surface waves are generated at the edges of basins near the base of the SGM; these surface waves cause the strong resonance in the basins lasting beyond 100 sec. The purple arrow at 40 sec shows approximately the polarization of fault-generated Rayleigh wave and the orientation of the basin edge.

a significant part of which is carried by fault-generated surface waves, is reduced by the topography (caused by the scattering).

### Discussion and Conclusions

The effects of topography on the propagation of surface waves are significant. Large mountains surrounding basins can act as a natural seismic insulator by scattering the surface waves generated by earthquakes outside the basin. We have used a simple source model to isolate the effect on the ground

motion created by the SGM. However, our principal result is more general: The scattering of fault-generated surface waves by the topography of the SGM leads to less-efficient excitation of the basins at the basin edges. As the natural resonances in the basins are independent of the source model itself, as long as significant surface waves are generated by rupture on the Mojave segment of the SAF, the SGM will partially shield the LAB from strong ground motions. If most of the slip on the fault is deep and no significant surface waves are generated, then the topography will have a much smaller effect. If shallow earthquakes occur inside the basin,

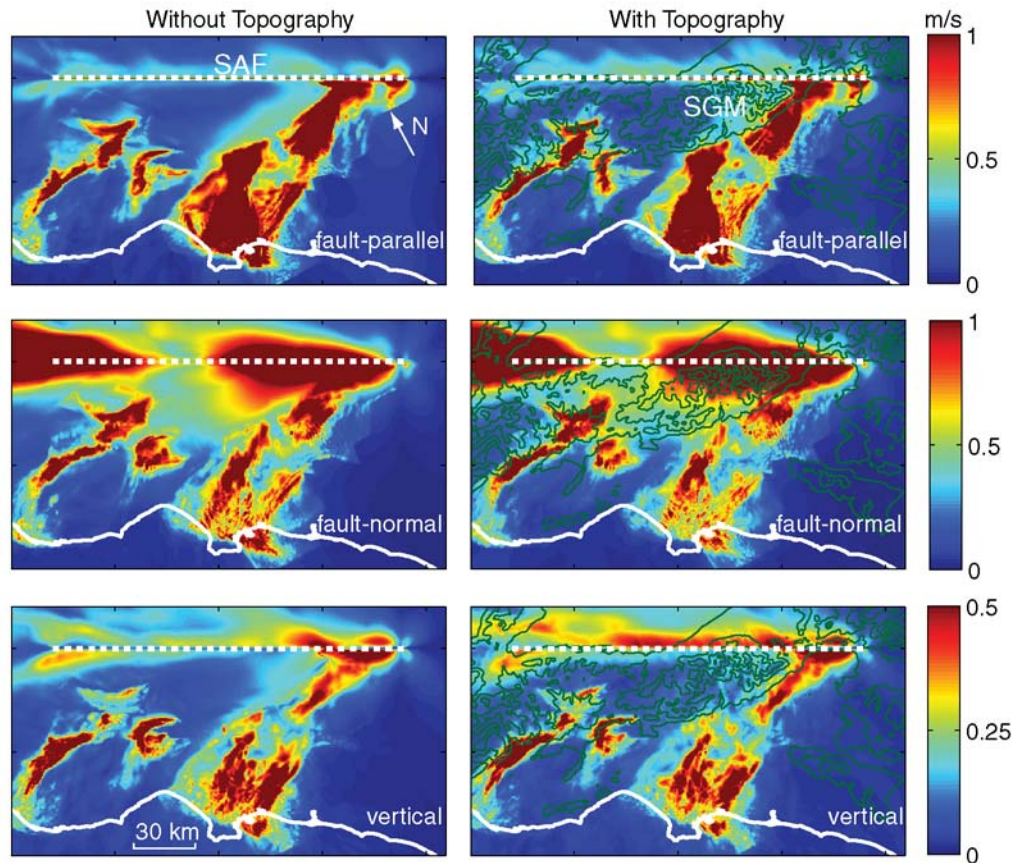


**Figure 10.** Comparison of peak ground velocities without surface topography (left-hand column) and with topography (right-hand column) in the 3D velocity model. The amplitude scale is saturated. The similarity between the distributions of peak ground velocities with and without topography indicates that ground motion is dominated by the subsurface velocity structure.

the surface topography surrounding the basin can increase the ground motion in the basin by reflecting the energy back into the basin, as seen for the energy reflected by the SGM into the Mojave. A counterexample to the SGM in Los Angeles would be the San Bernardino Mountains (SBM; Fig. 1), where most of the mountain ranges are on the northeast side of the SAF. The effect of the SBM on the propagation of surface waves from the SAF and the ground motion in the LAB will be a subject of future research.

We point out that any surface irregularities, not only mountains but also canyons, trenches, and other concave features, could affect the propagation of surface waves. The Earth's surface is not locally flat. If a large earthquake occurs in Southern California, we can imagine that the large topographic features surrounding Los Angeles will significantly scatter the surface waves, which usually dominate the peak amplitude of low-frequency ground motion, and in turn affect the ground motion in the basins. As we have shown in Figure 5, even when the dimension of the topographic feature is an order of magnitude smaller than the wavelength of the incident surface wave, there are still considerable effects. In addition to its clear ramifications for seismic hazard in the Los Angeles region, our simulations help to

explain the difficulty of predicting ground motions without taking into account topographic effects. For example, in the 1971 San Fernando earthquake, Vidale and Helmberger (1988) showed that simulated Rayleigh waves in the LAB were much larger than the measured data in models that neglected the Santa Monica Mountains. Our simulations would certainly support the argument that large surface topographic features should be taken into account for seismic hazard analysis.

### Acknowledgments

We thank Bodo Bookhagen for providing the digital elevation data and Dimitri Komatitsch for providing his code for generating a plane Rayleigh wave and sharing digitized solutions of Sánchez-Sesma (1983). We had a lot of helpful discussions with Chen Ji, Toshiro Tanimoto, and Greg Beroza. Two anonymous reviewers' comments greatly improved the manuscript. This work is supported by the Southern California Earthquake Center (SCEC), by NSF ITR through Award Number EAR-0122464 (The SCEC Community Modeling Environment [SCEC/CME]: An Information Infrastructure for System-Level Earthquake Research), and by IGPP LANL Grant Number 04-08-16L-1532. SCEC is funded by NSF Cooperative Agreement Number EAR-0106924 and U.S. Geological Survey Cooperative Agreement Number 02HQAG0008. This is SCEC Contribution Number 1087 and Institute for Crustal Studies Contribution Number 0805.

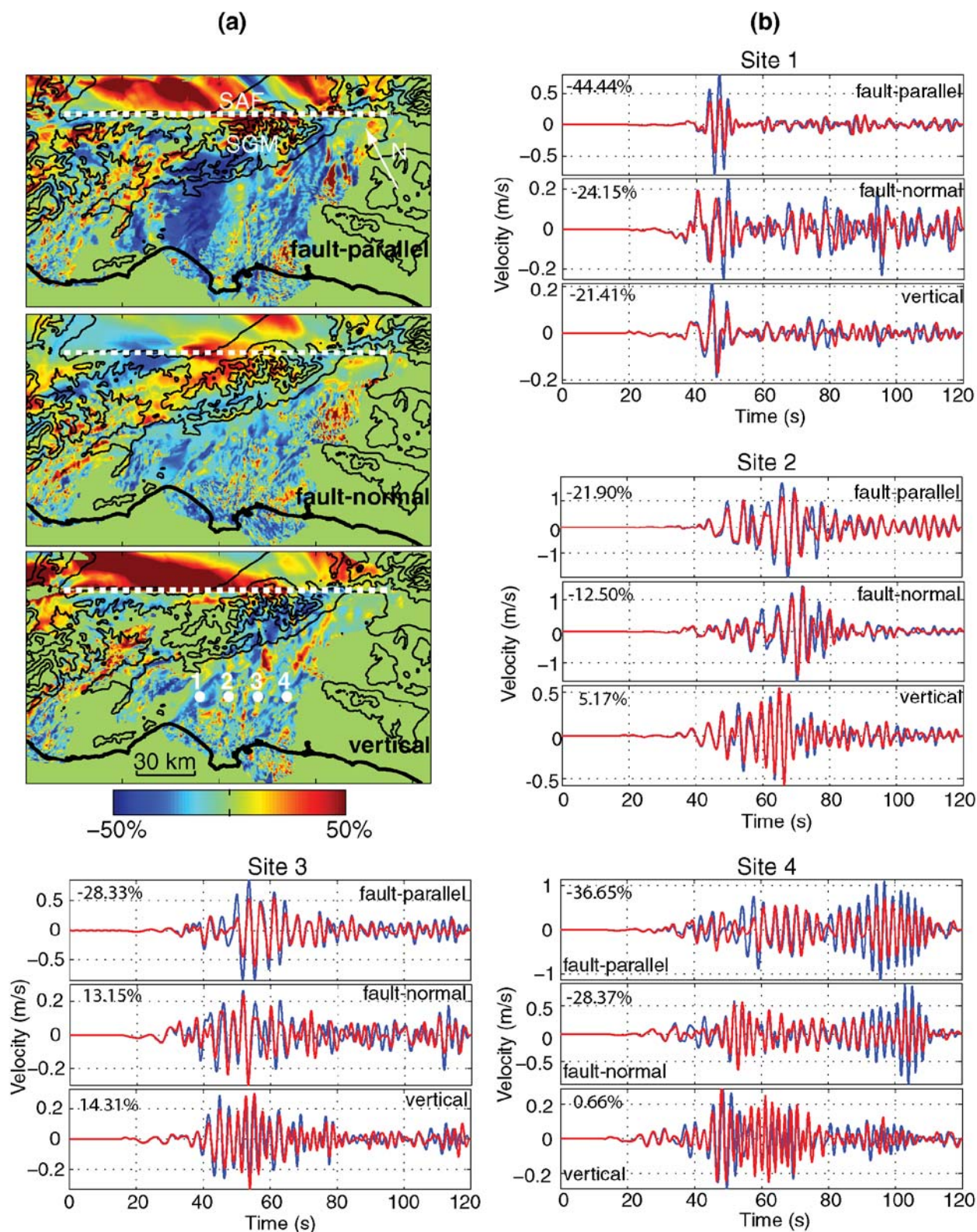


**Figure 11.** (a) Maps of the relative change in peak ground velocity from simulations with and without topography ( $(V^{topo} - V^{notopo}) / V^{notopo}$ ) in the 3D velocity model at locations for which the peak velocity without topography is greater than 0.1 m/sec. When peak velocity—without topography—is less than 0.1 m/sec, the relative change is set at zero. The white dots in the bottom panel denote the four sites where we plot the seismograms in (b). (b) Comparison of velocity time histories with (red) and without (blue) topography in the 3D velocity model at the four sites denoted in (a). The relative change in peak velocity—with and without topography—is shown at the upper left of each trace.

## References

- Angot, A. (1910). Le tremblement de terre du 11 juin 1909 dans le Sud-Est de la France, I, Enquête du Bureau Central Météorologique, *Ann. Géogr.* **103**, 8–15.
- Archuleta, R. J., and S. H. Hartzell (1981). Effects of fault finiteness on near-source ground motion, *Bull. Seismol. Soc. Am.* **71**, 939–957.
- Assimaki, D., G. Gazetas, and E. Kausel (2005). Effects of local soil conditions on the topographic aggravation of seismic motion: parametric investigation and recorded field evidence from the 1999 Athens earthquake, *Bull. Seismol. Soc. Am.* **95**, 1059–1089.
- Bouchon, M., C. Schultz, and M. Toksoz (1996). Effect of three-dimensional topography on seismic motion, *J. Geophys. Res.* **101**, 5835–5846.
- Brambati, A., E. Faccioli, G. B. Carulli, F. Cucchi, R. Onofri, S. Stefanini, and F. Ulcigrai (1980). Studio de microzonazione sismica dell'area di Tarcento (Friuli), Regione Autonomia Friuli-Venezia Giulia and Università degli Studi di Trieste con la collaborazione del Politecnico di Milano, Trieste.
- Çelebi, M., and T. Hanks (1986). Unique site response conditions of two major earthquakes of 1985: Chile and Mexico, in *Proceedings of the International Symposium of Engineering Geology Problems in Seismic Areas*, Bari, Italy, April 1986, Vol. IV.
- Day, S. M., and C. R. Bradley (2001). Memory efficient simulation of anelastic wave propagation, *Bull. Seismol. Soc. Am.* **91**, 520–531.
- Fialko, Y. (2006). Interseismic strain accumulation and the earthquake potential on the southern San Andreas fault system, *Nature* **441**, 968–971, doi 10.1038/nature04797
- Frankel, A., and J. Vidale (1992). A three-dimensional simulation of seismic waves in the Santa Clara Valley, California, from a Loma Prieta aftershock, *Bull. Seismol. Soc. Am.* **82**, 2045–2074.
- Frankel, A. D., M. D. Petersen, C. S. Mueller, K. M. Haller, R. L. Wheeler, E. V. Leyendecker, R. L. Wesson, S. C. Harmsen, C. H. Cramer, D. M. Perkins, and K. S. Rukstales (2002). Documentation for the 2002 update of the National Seismic Hazard maps, *U.S. Geol. Surv. Open-File Rept.* 02-420.
- Fuyuki, M., and Y. Matsumoto (1980). Finite difference analysis of Rayleigh wave scattering at a trench, *Bull. Seismol. Soc. Am.* **70**, 2051–2069.
- Fuyuki, M., and M. Nakano (1984). Finite difference of Rayleigh wave transmission past an upward step change, *Bull. Seismol. Soc. Am.* **74**, 893–911.
- Geli, L., P.-Y. Bard, and B. Jullen (1988). The effect of topography on earthquake ground motion: a review and new results, *Bull. Seismol. Soc. Am.* **78**, 42–63.
- Graves, R. W. (1998). Three-dimensional finite-difference modeling of the San Andreas fault: source parameterization and ground-motion levels, *Bull. Seismol. Soc. Am.* **88**, 881–897.
- Hartzell, S. H., D. L. Carver, and K. W. King (1994). Initial investigation of site and topographic effects at Robinwood Ridge, California, *Bull. Seismol. Soc. Am.* **84**, 1336–1349.
- Jacoby, B., P. Sheppard, and K. Sieh (1988). Irregular recurrence of large earthquakes along the San Andreas fault: evidence from trees near Wrightwood, *Science* **241**, 196–199.
- Ji, C., S. Tsuboi, D. Komatitsch, and J. Tromp (2005). Rayleigh-wave multipathing along the west coast of North America, *Bull. Seismol. Soc. Am.* **95**, 2115–2124, doi 10.1785/0120040180.
- Kawase, H. (1988). Time-domain response of a semi-circular canyon for incident SV, P, and Rayleigh waves calculated by the discrete wavenumber boundary element method, *Bull. Seismol. Soc. Am.* **78**, 1415–1437.
- Komatitsch, D., Tromp, and J. (1999). Introduction to the spectral-element method for 3-D seismic wave propagation, *Geophys. J. Int.* **139**, 806–822.
- Komatitsch, D., and J. Tromp (2002a). Spectral-element simulations of global seismic wave propagation. I. Validation, *Geophys. J. Int.* **149**, 390–412.
- Komatitsch, D., and J. Tromp (2002b). Spectral-element simulations of global seismic wave propagation. II. Three-dimensional models, oceans, rotation and self-gravitation, *Geophys. J. Int.* **150**, 303–318.
- Komatitsch, D., Q. Liu, J. Tromp, P. Süß, C. Stidham, and J. H. Shaw (2004). Simulation of ground motion in the Los Angeles basin based upon the spectral-element method, *Bull. Seismol. Soc. Am.* **94**, 187–206.
- Krishnan, S., J. Chen, D. Komatitsch, and J. Tromp (2006). Case studies of damage to tall steel moment-frame buildings in Southern California during large San Andreas earthquakes, *Bull. Seismol. Soc. Am.* **96**, 1523–1537, doi 10.1785/0120050145.
- Liu, Q., J. Polet, D. Komatitsch, and J. Tromp (2004). Spectral-element moment-tensor inversions for earthquakes in southern California, *Bull. Seismol. Soc. Am.* **94**, 1748–1761.
- Lysmer, J., and R. L. Kuhlemeyer (1969). Finite dynamic model for infinite media, *J. Eng. Mech.* **95**, 859–877.
- Ma, S., and P. Liu (2006). Modeling of the perfectly matched layer absorbing boundaries and intrinsic attenuation in explicit finite-element methods, *Bull. Seismol. Soc. Am.* **96**, 1779–1794, doi 10.1785/0120050219.
- Magistrale, H., S. M. Day, R. W. Calyton, and R. Graves (2000). The SCEC southern California reference three-dimensional seismic velocity model version 2, *Bull. Seismol. Soc. Am.* **90**, S65–S76.
- Mal, A. K., and L. Knopoff (1965). Transmission of Rayleigh waves past a step change in elevation, *Bull. Seismol. Soc. Am.* **55**, 319–334.
- Munasinghe, M., and G. W. Farnell (1973). Finite difference analysis of Rayleigh wave scattering at a vertical discontinuities, *J. Geophys. Res.* **78**, 2454–2466.
- Olsen, K. B., and R. J. Archuleta (1996). Three-dimensional simulation of earthquakes on the Los Angeles fault system, *Bull. Seismol. Soc. Am.* **86**, 575–596.
- Olsen, K. B., R. J. Archuleta, and J. R. Matarese (1995). Three-dimensional simulation of a magnitude 7.75 earthquake on the San Andreas fault, *Science* **270**, 1628–1632.
- Olsen, K. B., S. M. Day, J. B. Minster, Y. Cui, A. Chourasia, M. Faerman, R. Moore, P. Maechling, and T. Jordan (2006). Strong shaking in Los Angeles expected from southern San Andreas earthquake, *Geophys. Res. Lett.* **33**, L07305, doi 10.1029/2005GL025472.
- Pitarka, A., K. Irikura, T. Iwata, and H. Sekiguchi (1998). Three-dimensional simulation of the near-fault ground motion for the 1995 Hyogo-Ken Nanbu (Kobe), Japan, earthquake, *Bull. Seismol. Soc. Am.* **88**, 428–440.
- Sánchez-Sesma, F. J. (1983). Diffraction of elastic waves by three-dimensional surface irregularities, *Bull. Seismol. Soc. Am.* **139**, 1621–1636.
- Shakal, A., M. Huang, and T. Cao (1988). The Whittier Narrows, California, earthquake of October 1, 1987: CSMIP strong motion data, *Earthq. Spectra* **4**, 75–100.
- Shakal, A., M. Huang, R. Darragh, T. Cao, R. Sherburne, P. Malhotra, C. Cramer, R. Sydnor, V. Graizer, G. Maldonado, C. Peterson, and J. Wampole (1994). CSMIP strong motion records from the Northridge, California, earthquake of 17 January 1994, *Calif. Div. Mines Geol. Rept. OSMS 94-07*.
- Sieh, K., M. Stuiver, and D. Brillinger (1989). A more precise chronology of earthquake produced by the San Andreas fault in southern California, *J. Geophys. Res.* **94**, 603–623.
- Siro, L. (1982). Southern Italy November 23 1980 earthquake, in *Proceedings of the 7th European Conference on Earthquake Engineering*, Athens, Greece, September 20–25.
- Spudich, P., M. Hellweg, and W. H. K. Lee (1996). Directional topographic site response at Tarzana observed in aftershocks of the 1994 Northridge, California, earthquake: implications for mainshock motions, *Bull. Seismol. Soc. Am.* **86**, no. 1B, S193–S208.
- Vidale, J., and D. V. Helmberger (1988). Elastic finite-difference modeling of the 1971 San Fernando, California earthquake, *Bull. Seismol. Soc. Am.* **78**, 122–141.

Wong, H. L. (1982). Effect of surface topography on the diffraction of P, SV, and Rayleigh waves, *Bull. Seismol. Soc. Am.* **72**, 1167–1183.

Working Group on California Earthquake Probabilities (1995). Seismic hazards in southern California: probable earthquakes, 1994 to 2024, *Bull. Seismol. Soc. Am.* **85**, 379–439.

## Appendix

### Validation of the Finite-Element Method

A classic test of wave propagation in the presence of surface topography is a hemispherical crater in a homogeneous half-space where a plane  $P$  wave is incident vertically. Sánchez-Sesma (1983) visited this problem and provided an approximate boundary solution. In our test, the  $P$ -wave velocity,  $S$ -wave velocity, and density for the homogeneous half-space are 1732 m/sec, 1000 m/sec, and 1000 kg/m<sup>3</sup>, respectively. The radius of the crater  $r$  is 1 km. To avoid the artifacts of the boundary conditions, our computational domain is 48 km long by 48 km wide by 24 km deep, where the absorbing boundary of Lysmer and Kuhlemeyer (1969) is implemented on all the boundaries except the free surface. A plane  $P$  wave with a shape of a Ricker wavelet is incident from the bottom of the domain. We solve the problem for two different incident frequencies:  $\sqrt{3}/4$  Hz and  $\sqrt{3}/8$  Hz, which correspond to wavelengths of  $4r$  and  $8r$ , respectively. The entire computational domain is discretized with a hexahedral element mesh, which is very similar to figure 14 in Komatitsch and Tromp (1999). The element size is approximately 10 m near the crater to accurately model the geometry of the crater and increases gradually to about 240 m near the boundary. The simulation uses a total of 12,160,501 nodes and 12,000,000 elements.

To simulate a vertically incident plane  $P$  wave, instead of implementing the periodic boundary condition we analytically calculate the tractions along the free surface due to the incident  $P$  wave. We apply the same tractions with the sign reversed at the free surface (the total traction must be zero to satisfy the free surface boundary condition) and use the finite-element method (Ma and Liu, 2006) to calculate the reflected wave field. The total wave field is the sum of the incident and the reflected wave fields. The computation of the reflected wave field is performed in the time domain with a timestep of 0.01 sec and a duration long enough such that the velocity in the region of interest goes to zero. The time histories at the surface are then converted to the frequency domain, and the Fourier amplitudes at the incident frequency are calculated and normalized by the Fourier amplitude of the incident wave at the incident frequency in order to compare with the solutions of Sánchez-Sesma (1983).

Figure A1 shows the comparisons between the finite-element solutions and the solutions of Sánchez-Sesma (1983) for the two different incident frequencies. The finite-element solutions clearly reproduce the amplification pattern at the surface due to the crater. The excellent agree-

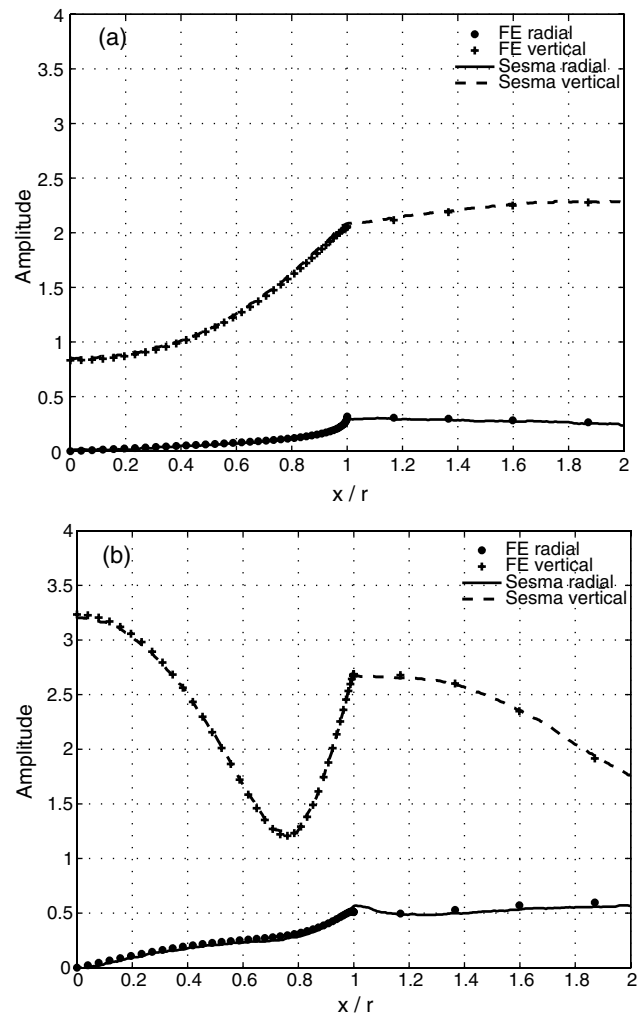


**Figure A1.** Comparison between the finite-element solution and the approximate boundary solution of Sánchez-Sesma (1983) for the Fourier amplitudes at the incident frequency of (a)  $\sqrt{3}/8$  Hz and (b)  $\sqrt{3}/4$  Hz at the surface as a function of the horizontal distance to the origin of the crater  $x$  normalized by the radius of the crater  $r$ . Both the radial and vertical amplitudes of the finite-element solution are normalized by the Fourier amplitude of the incident  $P$  wave at each incident frequency. The tangential component is zero due to the symmetry of the problem.

ment demonstrates the accuracy of the finite-element method in computing wave propagation with surface topography.

Department of Earth Science and Institute for Crustal Studies  
University of California  
Santa Barbara, California 93106  
(S.M., R.J.A.)

Department of Physics  
University of California  
Santa Barbara, California 93106  
(M.T.P.)